First evidence and characterization of strain-induced crystallization heterogeneity in natural rubber under homogeneous strain states

Jean-Benoit Le Cam, Adel Tayeb, Sylvain Charles

CRediT author statement

Jean-Benoit Le Cam: Conceptualization, Methodology, Original draft preparation, Writing, Reviewing, Editing, Supervision. **Adel Tayeb**: Writing, Reviewing, Investigation, Software. **Sylvain Charlès:** Visualization, Investigation, Software.

Heterogeneity of strain-induced crystallization during a homogeneous uniaxial tensile test

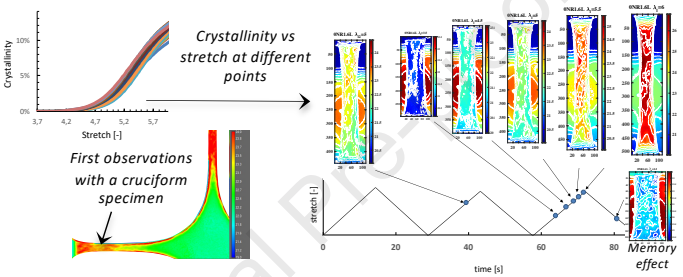

First evidence and characterization of strain-induced crystallization heterogeneity in natural rubber under homogeneous strain states

J.-B. Le Cam, [a,1] Adel Tayeb, [a] Sylvain Charlès [a]

[a] *Université de Rennes 1, Institut de Physique UMR 6251 CNRS/Université de Rennes 1, Campus de Beaulieu, Bât. 10B, 35042 Rennes Cedex, France.*

Abstract

This paper provides the first evidence of strain-induced crystallization heterogeneities at the macroscopic scale, accompanied with strong memory effects during uniaxial cyclic tensile loadings in unfilled natural rubber. Specimens with two different sulfur amounts, 1.2 phr and 1.6 phr, and two different geometries, small and large widths, have been considered. The crystallinity has first been evaluated in the middle of each specimen thanks to a quantitative surface calorimetry approach based on infrared thermography. The calorimetric approach was then used to simultaneously access the crystallinity at different points of the tested specimens and to investigate spatial variations in the crystallinity along a profile at the middle of each specimen. SIC was found to occur heterogeneously along the profile, i.e. at the macroscopic scale, whatever the geometry and the sulfur amount are. Moreover, crystallization and melting initiate in the same zones during load-unload cycles. Several families in terms of heat sources due to SIC have been identified.

Key words: strain-induced crystallization, macroscopic SIC heterogeneity, natural rubber, infrared thermography, surface calorimetry.

1 Introduction

The strain-induced crystallization (SIC) is considered as the phenomenon responsible for the extraordinary properties of natural rubber (NR). Even though SIC has been intensively investigated since the pioneering work by

[1] Corresponding author jean-benoit.lecam@univ-rennes1.fr Fax : (+33) 223 236 111

Katz (1925), especially by means of the X-ray diffraction technique (Bunn, 1942; Takahashi and Kumano, 2004; Immirzi *et al.*, 2005; Rajkumar *et al.*, 2006; Goppel and Arlman, 1949; Toki *et al.*, 2000; Trabelsi *et al.*, 2003), it is still misunderstood and remains the subject of many investigations. For instance, the mechanism by which the fatigue life of crystallizable rubbers is reinforced under non-relaxing conditions is not clear. SIC is generally invoked in the literature (Cadwell *et al.*, 1940; Saintier, 2000; Saintier *et al.*, 2006; Le Cam *et al.*, 2004, 2008; Le Cam and Toussaint, 2010; Beurrot *et al.*, 2010; Le Cam *et al.*, 2013; Rublon *et al.*, 2014; Ruellan *et al.*, 2018, 2019), but without any evidence having been provided to date, other than the fact that non-crystallizable rubbers do not undergo such reinforcement. At the macromolecular scale, SIC depends on the local network density (Tosaka, 2009; Suzuki *et al.*, 2010; Ikeda *et al.*, 2009; Toki *et al.*, 2003; Toki and Hsiao, 2003; Vieyres *et al.*, 2013; Valentin *et al.*, 2010; Qin and G. B. McKenna, 2006). It has been established that the higher the network chain density, the lower the crystallite size (Trabelsi *et al.*, 2003; Tosaka *et al.*, 2004; Chenal *et al.*, 2007). The size limiting phenomenon is however not clear and Candau *et al.* (2014) support the idea that SIC would correspond to the successive appearance of crystallite populations, which nucleation and growth would depend on the local network density. In order words, SIC is mainly governed by the local distribution in the network density. This is in a good agreement with Tosaka *et al.* (2004) who previously showed that for a given ratio of accelerator over sulphur (0.67), increasing the sulphur amount so that the network-chain density ν increases from 1.01 10^{-4} to 2.12 10^{-4} mol/cm^3 increases the crystallinity rate. Later, Chenal *et al.* (2007) investigated the effect of ν in a range between 0.23 10^{-4} and 1.95 10^{-4} mol/cm^3 by changing the accelerator amount for the same sulphur amount and found that the crystallinity rate knew a maximum value for ν equal to 1.2 10^{-4} mol/cm^3, which corroborates the data they extracted from Trabelsi *et al.* (2003).

At the macroscopic scale at which the media is considered as a continuum, these effects are assumed to be averaged and the main effects that affect SIC for a given chemical formulation is generally the stretch level and the temperature (Flory, 1947; Marchal, 2006). Crystallization induced by a homogeneous strain state, which is typically the case of uniaxial tension loadings with constant cross-section specimens, is therefore assumed to take place homogeneously at the macroscopic scale (see the reviews on SIC by Huneau (2011) and Yijing *et al.* (2017)) and the crystallinity is evaluated at one point with the XRD technique (see Toki *et al.* (2000); Albouy *et al.* (2012, 2014); Trabelsi *et al.* (2003); Poompradub *et al.* (2005); Kohjiya *et al.* (2007) for uniaxial tensile loadings and Beurrot *et al.* (2011); Chen *et al.* (2019) for biaxial loadings). The spatial resolution of the XRD measurements is given by a spot size ranging between several hundreds of microns and 1 mm in diameter (Candau *et al.*, 2014; Le Cam *et al.*, 2020). The crystallinity is averaged over the spot size. The very few studies investigating heterogeneous crystallinity deal systematically with heterogeneous strain states. Typically, Trabelsi *et al.* (2002) and

Rublon *et al.* (2013, 2014) measured the crystallinity in different zones in the vicinity of a stretched crack tip with the XRD technique. The strong gradient in the crystallinity from one zone to another were mainly associated with a strong gradient in the maximum stretch applied rather than the strain state, as it is mainly uniaxial. Moreover, the XRD patterns are not acquired at the same time from one point to another in the field and the spatial resolution leads to strong limitations when increasing the singularity level in the field.

To summarize, macroscopic heterogeneities in the crystallinity field are assumed to be due to the mechanical state, i.e. the strain state and level, not to other factors. As a consequence, if the strain field is homogeneous, so is considered the macroscopic crystallinity field. Macroscopic SIC heterogeneities as well as memory effects under homogeneous strain states have never been investigated at the macroscopic scale in the literature.

In the present study, preliminary observations on SIC with the infrared thermography (IRT) technique carried out during biaxial tests are first reported in Section 2. They highlight SIC heterogeneities at the macroscopic scale and motivate further investigations with dedicated uniaxial tests. Then, the theoretical formalism applied to determine the strain-induced crystallinity from quantitative surface calorimetry is presented in Section 3. The experimental setup is presented in Section 4: the uniaxial cyclic tensile loadings applied, the two materials with two different geometries considered, the thermal measurement and the movement compensation of points in the infrared (IR) images carried out. The results obtained are presented and discussed in Section 5. Concluding remarks close the paper.

2 Preliminary results and motivations for the present study

First observations made in our group about SIC heterogeneities under homogeneous strain field were carried out during equibiaxial tensile tests performed with cruciform unfilled natural rubber specimens of different sizes. Such tests enable us to investigate the effects of multiaxial strain states on SIC (Khiem *et al.*, 2022), as it gathers simultaneously a wide range of strain states in the specimen (Promma *et al.*, 2009): the specimen centre is submitted to equibiaxial tensile conditions, the branches to uniaxial tensile, and pure shear takes place in between (see biaxiality fields determined from kinematic field measurements in Fig. 13(d) in Promma *et al.* (2009) or in Fig. 7(a) in Tayeb *et al.* (2021)). The overview of the experimental setup is given in Figure 1. Note that this type of biaxial tensile test is increasingly used for characterizing the rubber behavior and for identifying constitutive parameters, with or without the use of additional measurements (full kinematic and/or thermal field(s)) (Guélon *et al.*, 2009; Johlitz and Diebels, 2011; Seibert *et al.*, 2014; Charlès

and Le Cam, 2020; Bastos *et al.*, 2021; Tayeb *et al.*, 2021).

Fig. 1. Overview of the experimental setup

During the tests, full thermal field measurements are performed with a cooled infrared camera. Figure 2 gives an example where the specimen is filmed on one side by a high thermal resolution FLIR IR camera [2] and by a CCD camera on the other side. The spatial resolution of the IR camera was equal to 0.465 mm/px. The prescribed displacement and the displacement rate for each branch end were equal to 200 mm and 150 mm/min, respectively. This leads to a maximum principal stretch in the branch much higher than the SIC onset (around 4). The stretch is defined as the current length over the initial length in a given direction. For instance, for a prescribed displacement of 189 mm in each branch, the maximum principal stretch is equal to 5.1. Figure 3 presents the mechanical response obtained in terms of normalized force versus global stretch obtained at the fifth cycle. The global stretch is calculated as the total length reached in each perpendicular direction over the initial length. In this figure, IR images show the temperature field at the specimen's surface at different times during the cycle.

At the beginning of the loading, the branches and the radius of curvature in between appear much colder than the rest of the specimen (see images L1

[2] The IR camera's features are precisely detailed in Section 4.3

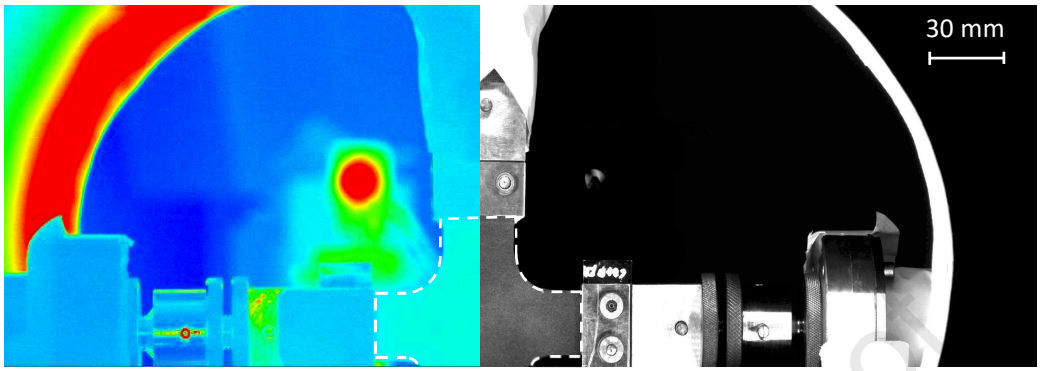

Fig. 2. The underformed specimen. Visible image on the right hand side. IR image on the left hand side.

and L2). This strong cooling is explained by the fact that the same amount of heat produced during the previous cycle due to crystallization has been absorbed during the previous unloading. The test conditions being non-adiabatic, the zone that crystallized and melted appears colder at the end of the first and second unloadings. The effect of non-adiabaticity on temperature variation during mechanical cycle for a natural rubber has been fully discussed in Samaca Martinez *et al.* (2013a) and the reader can refer to this paper for further information. From a certain macroscopic stretch level on, SIC occurred in the radii of curvature between the branches and strongly heats the material (image L4, corresponding to a prescribed displacement of 189 mm, for which the maximum principal stretch reached in the branch is 5.1), before extending in the branches (image L5). This is in a very good agreement with what Toussaint *et al.* (2012) observed with a natural rubber and a 3-branch specimen. At the beginning of the unloading, the zones where crystallization took place remained at quite the same temperature (image U1), which is consistent with the fact that crystallinity at the beginning of the unloading is superior to that during loading for a given stretch level. For lower stretches, melting occurred and decreased significantly the temperature of zones that have crystallized during the loading (images U2 to U6). At the end of the unloading, the thermal field was similar to that observed at the very beginning of the loading, in other words image U6 is similar to image L1. The deformation being also the same, this third cycle is therefore a thermodynamical cycle (see Chrysochoos *et al.* (2010) for further information).

In the following, we focus on images corresponding to the beginning of the

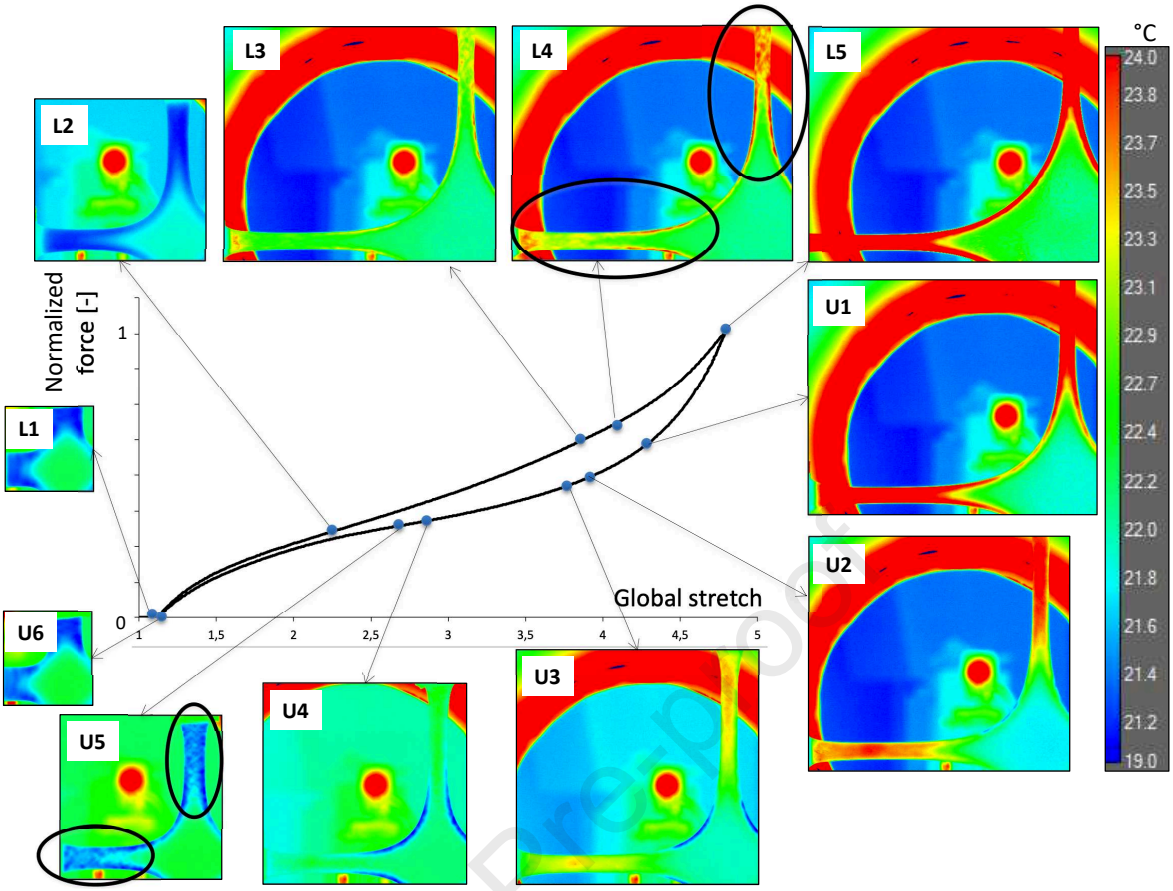

Fig. 3. Temperature fields at different times during the stabilized cycle

crystallization (image L4) and the end of the melting (image U5), and more especially in the encircled zone of the horizontal branches. Figure 4 provides a zoom-in of these zones as well as the temperature profile along the branch.

Clearly, this figure shows that the temperature fields are strongly heterogeneous when crystallization started and when melting was finishing. Moreover, this heterogeneity was only detected in crystallizing zones. As above-mentioned, macroscopic SIC heterogeneity is assumed to be due to strain state and level. So, the question is to know whether or not the heterogeneities observed in the temperature field are due to heterogeneities in the strain field. To answer this question, a finite element simulation of the test has been carried out. Results are given in Figure 5.

Fig. 5(b) provides the maximum principal stretch in the branch. Fig. 5(c) gives the biaxiality coefficient mapped in the branch. This coefficient enables us to determine the strain state at a given point and is calculated as $\frac{ln\lambda_{II}}{ln\lambda_I}$. λ_I and λ_{II} are the maximum and minimum in-plane principal stretches in the loading plane, respectively. These two figures clearly highlight that no heterogeneity is observed in the strain fields, even at stretches higher than the SIC onset (image L3). Furthermore, the stretch level reached is superior to

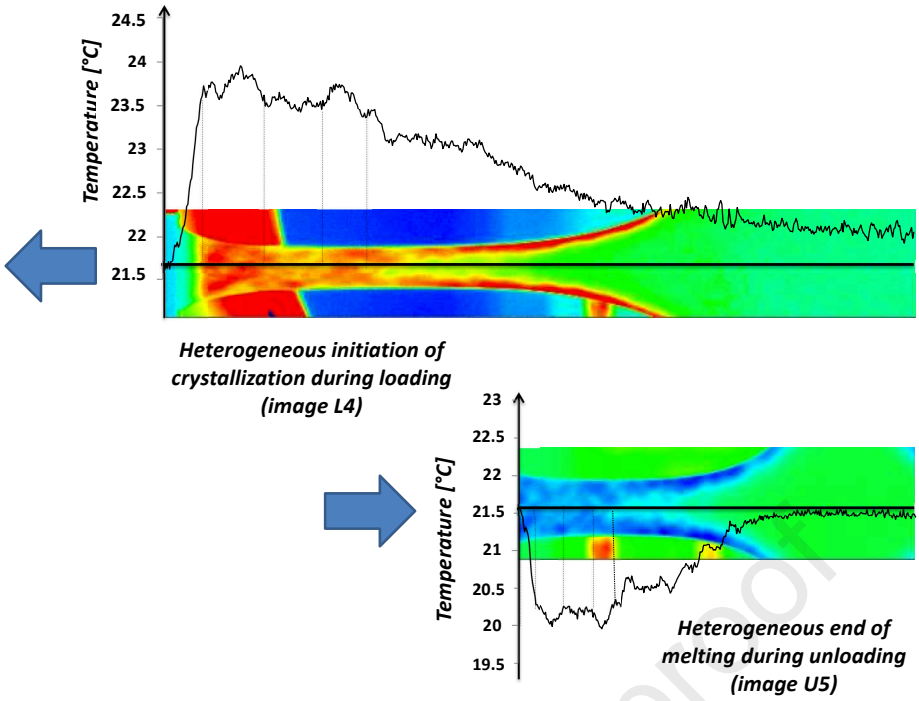

Fig. 4. Temperature profiles in the encircled zones in Fig. 3. The thermal field at the beginning of the crystallization during loading appears at the top, the thermal field close to the end of melting appears at the bottom.

that at which crystallization starts in unfilled natural rubber (around 4.2, see for instance Trabelsi *et al.* (2003)). This suggests that the SIC phenomenon took place heterogeneously at the macroscopic scale while the strain state is homogeneous at this scale. Such observations have been made many times in our group with different unfilled natural rubber formulations.

To finish, Image L4 corresponding to the beginning of the crystallization has been rescaled in order to be compared with Image U5 corresponding to the end of melting. It is presented in Fig. 6(a). It is observed that the morphology of the crystallizing and the melting zones are in a strong analogy. In order to quantitatively compare them, temperature profiles along the same line corresponding to the median axis of the branch has been extracted from the two images. They are reported in Fig. 6(b). This figure clearly shows that the temperature gradient zones are localized exactly at the same place. This means that areas that produce the largest heat amount during loading are those that also absorb the largest heat amount during unloading. As the macroscopic strain state should be homogeneous in these zones, SIC heterogeneity could be the main explanation for these observations. To go further on this memory-like effect, IR images taken during the second and third loads at the same maximum stretch are presented in Figure 7. The strong similitude between these two IR images confirms this memory effect, which has never been reported at the macroscopic scale in the literature.

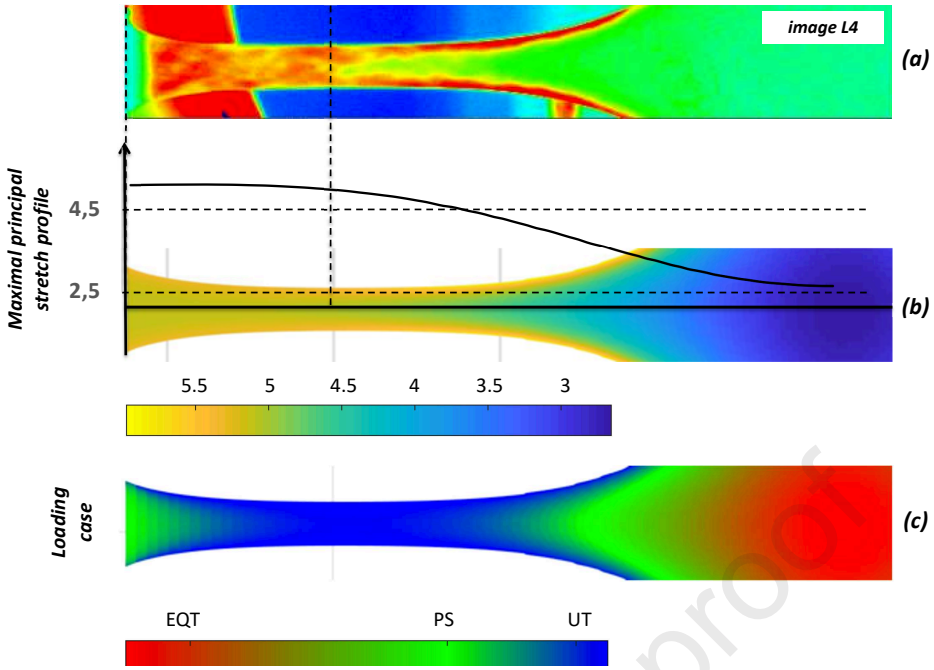

Fig. 5. Finite element simulation (a) maximum principal stretch field (b) and biaxiality coefficient field (c) for a global stretch equal to 4.15, corresponding to Image U4. EQT, PS, and UT stand respectively for EQuibiaxial Tension, Pure Shear and Uniaxial Tension. It clearly appears that in the zone where temperature gradients are observed, the strain state is homogeneous.

2.1 Discussion and motivations for further investigating SIC heterogeneities

SIC heterogeneity is widely evoked and evidenced at the macromolecular network scale, typically in terms of the crystallite size distribution as described in Huneau (2011) or Candau *et al.* (2014), but has never been investigated at the macroscopic scale. The preliminary observations we made clearly highlight that SIC heterogeneity and memory effects can be observed at the macroscopic scale under a homogeneous strain state. This questions on the origin of this heterogeneity, since it echoes to what is observed at the microscopic scale. Numerous questions arising on the origin of this heterogeneity. To go further more simple tests with unfilled natural rubber under uniaxial tensile loadings have to be performed. Moreover, as the tests are performed under non-adiabatic conditions, temperature measurements are affected by conducto-convective effects and temperature variations are not due to the material deformation only. Therefore, a more intrinsic quantity has to be considered to further investigate the thermomechanical response. In this study, the thermal fields are processed with the heat diffusion equation to determine the heat source field. This technique is well suitable as crystallinity can be obtained from the heat source variation at any point, as shown in Le Cam (2018) and Le Cam *et al.* (2020). Furthermore, temperature of each point of the field is obtained at the

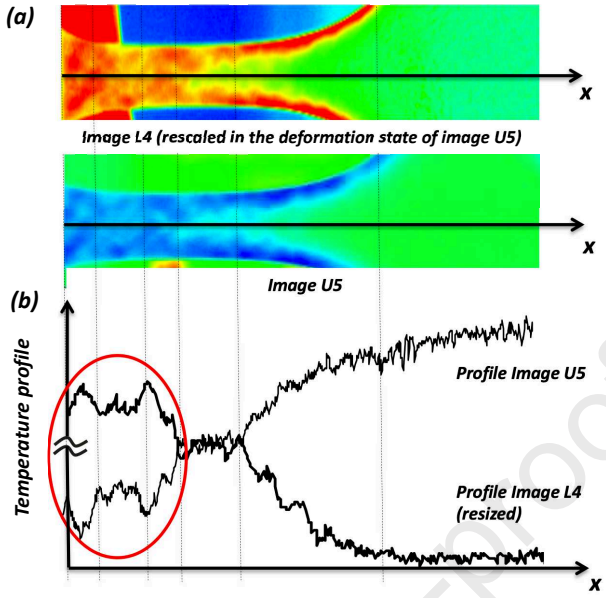

Fig. 6. Zones where SIC started and melting finished are the same (a) IR images L4 resized and U5 (b) Temperature profiles. The singularities are located at the same regions when SIC started and melting finished.

same time, meaning that the crystallinity field is not affected by SIC variation if the crystallinity is not evaluated at the same time from one point to another. Therefore, this technique is more suitable than the XRD technique to investigate SIC heterogeneity at the macroscopic scale. In the following, the methodology for evaluating the crystallinity from quantitative calorimetry is recalled. Then, the experimental setup is described and results obtained in terms of SIC heterogeneity at the macroscopic scale are presented and discussed.

3 Determining the strain-induced crystallinity from quantitative surface calorimetry

In this section, the theoretical framework for determining the heat sources from temperature measurements processed with the heat diffusion equation, is recalled. Then, the method for identifying the thermal energy due to SIC and evaluating the crystallinity is detailed.

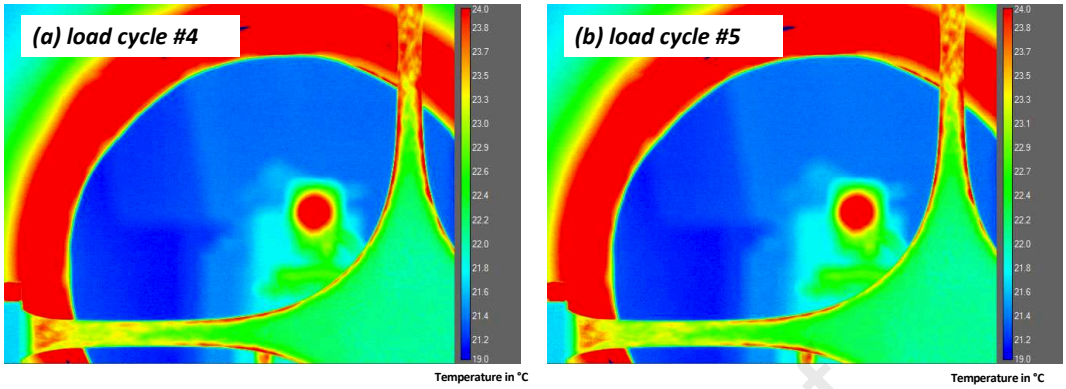

Fig. 7. IR images at the same global stretch (here 4.2) for the second and third loads. The IR images are almost superimposable as the similarities are huge.

3.1 Theoretical framework

Quantitative surface calorimetry (QSC) lies in the determination (the reconstruction) of the heat power density, also called heat source, from temperature measurements at the surface of a material and the heat diffusion equation (Chrysochoos, 1995). If the thermal measurement provides bidimensional fields, typically when using an infrared (IR) camera at the flat surface of a specimen, the tridimensional formulation of the heat diffusion equation has to be simplified accordingly (Chrysochoos *et al.*, 2010). This is all the more justified if the heat sources are homogeneous.

3.2 Tridimensional heat diffusion equation

In the case where the constitutive state equations are derived from the Helmholtz free energy function and that heat conduction follows Fourier's law, the mixed

formulation of the local heat diffusion equation writes as follows:

$$\rho_0 C\dot{T} + \mathrm{Div}\mathbf{Q} - R \;=\; \underbrace{\mathcal{D}_{int} + T\frac{\partial \mathbf{P}}{\partial T} : \dot{\mathbf{F}} + T\sum_{\beta=1}^{m} \frac{\partial \boldsymbol{A_\beta}}{\partial T} : \dot{\boldsymbol{\xi}}_{\boldsymbol{\beta}}}_{\hat{S}} \tag{1}$$

with ρ_0 the initial density, C the heat capacity, T the absolute temperature, $\mathbf{Q}$ the heat flux per unit reference area, R the external heat source (radiation, for instance), $\mathcal{D}_{int}$ the intrinsic dissipation (also named mechanical dissipation), $\mathbf{P}$ the first Piola-Kirchhoff stress tensor (or nominal stress tensor), $\mathbf{F}$ the deformation gradient tensor. $\hat{S} = \mathcal{D}_{int} + T\frac{\partial \mathbf{P}}{\partial T} : \dot{\mathbf{F}} + T\sum_{\beta=1}^{m} \frac{\partial \boldsymbol{A_\beta}}{\partial T} : \dot{\boldsymbol{\xi}}_{\boldsymbol{\beta}}$ denotes the heat source. The superposed dot stands for the material time derivative. Note that $\mathbf{Q} = -\boldsymbol{K_0}\mathbf{C}^{-1} det\mathbf{F}\mathrm{Grad}\, T$, where $\boldsymbol{K_0}$ is the thermal conductivity tensor and $\mathbf{C} = \mathbf{F}^T\mathbf{F}$ is the right Cauchy-Green tensor.
In the right member, the term $T\frac{\partial \mathbf{P}}{\partial T} : \dot{\mathbf{F}}$ is the heat sources due to the entropic and isentropic couplings. The term $T\frac{\partial \boldsymbol{A_\beta}}{\partial T} : \dot{\boldsymbol{\xi}}_{\boldsymbol{\beta}}$ corresponds to the other thermomechanical couplings. $\boldsymbol{\xi_\beta}$ are the internal tensorial variables, while $\boldsymbol{A_\beta}$ denote the corresponding thermodynamic forces.

3.3 Simplification of the heat diffusion equation

3.3.1 2D formulation

The temperature fields provided by IR thermography are bidimensional. Reconstructing the heat source field from them requires therefore the formulation of a two-dimensional version of the heat diffusion equation. To this end, several assumptions have to be made. Typically, the heat conduction is considered as isotropic (the thermal conductivity coefficient is denoted k_0 in the following), the material as incompressible, and the temperature as constant over the specimen thickness. If the specimen is relatively thin, Eq. (1) can be integrated over the thickness [3], which leads to the following two-dimensional formulation of the heat diffusion equation

$$\rho_0 C\left(\dot{T} + \frac{T - T_{amb}}{\tau_{2D}}\right) - \mathrm{Div}_{2D}(k_0\mathbf{C}^{-1}\mathrm{Grad}_{2D}\, T) - R \;= \hat{S}, \tag{2}$$

where T_{amb} is the ambient temperature. τ_{2D} is a time characterizing the heat exchanges along the thickness direction by convection with the air at the specimen surface. If the external radiations R are constant during the deformation process, they can be removed from the heat diffusion equation by using the

[3] The relevancy of this assumption (homogeneous temperature in the thickness direction) for a given situation can be evaluated by calculating the Biot number B_i (Louche, 2009).

temperature variation $\theta(X,Y,t) = T(X,Y,t) - T_{ref}(X,Y)$ instead of the temperature itself. It should be noted that T_{ref} is the ambient temperature if it is constant over the test. In this case, Eq. (2) writes:

$$\rho_0 C \left(\dot{\theta} + \frac{\theta}{\tau_{2D}} \right) - \mathrm{Div}_{2D}(k_0 \mathbf{C}^{-1} \mathrm{Grad}_{2D}\, \theta) = \hat{S}. \tag{3}$$

For the sake of simplicity, τ_{2D} is denoted τ in the following. τ can be characterized from a natural return to room temperature after a heating (or a cooling) for each testing configuration (machine used, environment, etc). Indeed, in this case $\theta = \theta_0 e^{\frac{-(t-t_0)}{\tau}}$. Either τ is determined at different increasing stretches as done in Samaca Martinez *et al.* (2013b), or it can be obtained in the undeformed state and corrected according to its dependency on the stretch and the multiaxiality state as follows (Charlès and Le Cam, 2020):

$$\tau = \tau(\lambda_I, B) = \tau_0 \lambda_I^{-B-1}, \tag{4}$$

where $B = \frac{ln\lambda_{II}}{ln\lambda_I}$ denotes the biaxiality ratio, defined as the ratio of the logarithm of the minimum by the maximum in-plane principal stretches, respectively. Under equi-biaxial tension, pure shear, and uniaxial tension, B is equal to 1, 0 and -0.5, respectively.

3.3.2 "0D" formulation

In practice, for materials with low thermal diffusivity such as rubbers, in the case of homogeneous strain field the thermal gradient remains confined to the area close to the grips, i.e. heat conduction is negligible in the specimen plane and heat exchanges with the grips of the testing machine does not induce temperature gradient in the measurement zone, the two-dimensional heat diffusion equation can be simplified (Chrysochoos, 1995; Berthel *et al.*, 2008) and corresponds to the "0D" formulation of the heat diffusion equation:

$$\rho_0 C \left(\dot{\theta} + \frac{\theta}{\tau} \right) = \hat{S}. \tag{5}$$

Elastomeric materials are generally assumed to be incompressible, i.e $\rho = \rho_0$. This equation applies for homogeneous heat source field, but also in the case of heterogeneous heat source field if the heat conduction is negligible. In the case where the material has a bad thermal conductivity, typically an elastomer, and that the stress gradient is low, the in-plane heat conduction is negligible. Here, τ_0 is characterized from the return to the ambient temperature of a heated undeformed specimen. The evolution of τ with the stretch is then determined with Equation 5 by setting B at -0.5. Indeed, a change in temperature of the material (heating or cooling) changes the crystallinity. Therefore,

an additional heat production or absorption is obtained during the return at the initial crystallinity, which affects the temperature variation during the return at ambient temperature and, consequently, the identification of τ_0. Finally, note that τ is determined without any displacement of the specimen in air. In the present paper, the specimens are stretched symmetrically in order to limit additional heat convection due to displacement of the measurement surface in air and to meet the same conditions as those for determining τ. Note finally that Equation 5 is formulated in the case where the ambient temperature T_{amb} is constant during the test. In case where changes in ambient temperature occur, the term $\frac{\theta}{\tau}$ has to be corrected accordingly and replaced by $\frac{T-T_{amb}}{\tau}$.

3.4 Evaluation of the crystallinity

The X-ray diffraction technique is generally used to investigate SIC as it provides the crystallinity level as well as information of paramount importance about crystallites sizes and orientations. Nevertheless, the measurement is performed at a single point, more precisely the measurement is averaged over the X-ray spot. Consequently, the crystallinity is not determined at the same time from one point to another. As crystallinity possibly evolves with time, we did not choose the XRD technique to investigate SIC heterogeneity in the present study. Moreover, the spot should have to be moved according to the movement of the measurement point, which appears very complicated. This is the reason why we did not choose this technique for investigating SIC heterogeneity. The calorimetric method developed in Le Cam (2018) overcomes this limitation, since the full crystallinity field can be deduced from the temperature field, which can be easily obtained using infrared thermography. The method has been validated by comparing with results obtained by the X-ray diffraction technique (Le Cam *et al.*, 2020). This method is applied to process the temperature variations of each point along the profile defined in Section 4.3. The method is illustrated in Figure 8, which gives the experimental heat source and the heat source predicted of an unfilled rubber. The first step of the method aims at measuring the total heat source produced by the material, by using the heat equation (see solid curve in Fig. 8). The second step of the method consists in predicting the heat source if no crystallization occurs. This is made by using the polynomial form (see the dashed curve in Fig. 8). The heat source due to SIC is then deduced by subtracting the heat source predicted for the third cycle, which is a thermodynamical cycle, from the total heat source. The equivalent temperature variation T_{cryst} can then be determined from the integration of the heat source due to SIC over time, and assuming that it is equal to 0 before the crystallization starts. Last, the crystallinity χ, which is the volume fraction of crystallites, is deduced from T_{cryst} and the fusion enthalpy ΔH_{cryst} as follows;

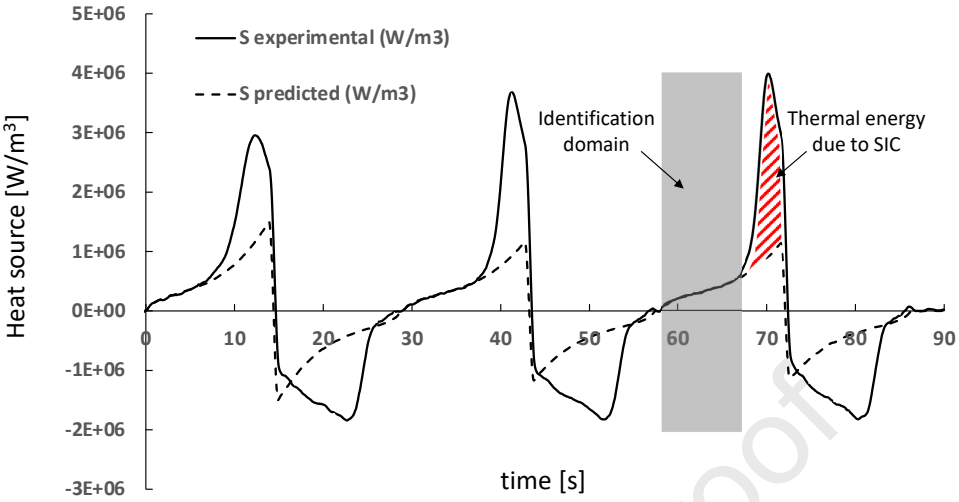

Fig. 8. Experimental heat source (solid line) and heat source predicted (dashed line) during the mechanical loading of specimen $NR_{1.2}S$. The identification of the predicted heat source due to elastic couplings is only carried out before SIC starts, i.e. in the temporal domain in grey, during the third (stabilized) cycle. The difference between the two curves is the thermal energy due to SIC.

$$\chi(t) = \frac{\rho C_p T_{cryst}(t)}{\Delta H_{cryst}} \tag{6}$$

The enthalpy of fusion is assumed to be independent of temperature and stretch. Here, as a first approach, we use the value determined by Roberts and Mandelkern (1955), and set it at 15.3 cal/g. The method has been validated by comparing with the X-ray technique in Le Cam *et al.* (2020).

4 Experimental set-up

4.1 Material and specimen geometry

In the present study, an unfilled natural rubber is considered, with two different sulphur amounts, 1.2 and 1.6 *phr* [4], since SIC is affected by the network chain density. They are denoted $NR_{1.2}$ and $NR_{1.6}$ in the following. They have been provided by The "Manufacture Française des pneumatiques Michelin". Their chemical composition is provided in Table 1.

Ingredient	$NR_{1.2}$	$NR_{1.6}$
NR (phr)	100	100
Zinc oxide (phr)	1.5	1.5
Sulphur (phr)	1.2	1.6
Accelerator (phr)	1.9	2.53
Stearic acid (phr)	2	2
Antioxidant (phr)	3	3

Table 1
Chemical composition of the two natural rubbers

Specimens with different widths have been used, one small and one large for each sulfur amount, as summarized in Table 2. The schematic view of the specimens' geometry is given in Figure 9. The specimens of smaller width were denoted $NR_{1.2}S$ and $NR_{1.6}S$, those of larger width $NR_{1.2}L$ and $NR_{1.6}L$. The mass density ρ was equal to 948.2 kg.m^3 and 957.6 kg.m^3 for $NR_{1.2}$ and $NR_{1.6}$, respectively. The heat capacity C as a function of temperature were given by $749 + 3.5T$ $J/(kg.K)$ and by $845 + 3.4T$ $J/(kg.K)$ for $NR_{1.2}$ and $NR_{1.6}$, respectively. T is the absolute temperature in K.

4.2 Loading conditions

The specimens were stretched in the vertical direction with the biaxial testing machine presented in Figure 1. It is composed of four independent electrical actuators with 1000 N load cells measuring the force in the two perpendicular directions and driven by an in-house LabVIEW program. This machine enables us to stretch symmetrically the specimens, which ensures a motionless specimen center, i.e. the middle section contracts along the horizontal

[4] parts per hundred parts of rubber in weight

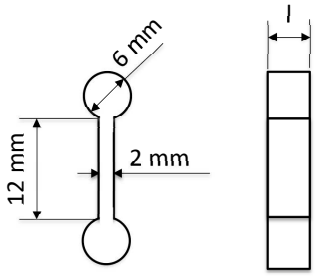

Fig. 9. Schematic view of the specimens'geometry

$NR_{1.2}$	$NR_{1.6}$	Geometry
L = 12 mm	L = 12 mm	
l = 9.64 mm	l = 8.36 mm	Small specimen
e = 2 mm	e = 2 mm	
L = 12 mm	L = 12 mm	
l = 18.8 mm	l = 16.1 mm	Large specimen
e = 2 mm	e = 2 mm	

Table 2
Dimensions of the different specimens used

direction, but does not move in the vertical direction. In the present case, the specimens were mounted in the vertical direction. The mechanical loading applied corresponded to three load-unload uniaxial tensile cycles at a maximum stretch of 7 and a loading rate of 300 mm/min.

4.3 Thermal measurement

Temperature measurement was performed by using a cooled high-resolution FLIR X6540sc infrared camera equipped with a focal plane array of 640x512 pixels and detectors operating in wavelengths between 1.5 and 5.1 μm. The integration time was equal to 2.7 ms. The acquisition frequency was equal to 20 Hz. The calibration of camera detectors was performed with a black body using a one-point NUC procedure at this acquisition frequency. The thermal resolution, i.e. the noise equivalent temperature difference (NETD), was equal to 20 mK for a temperature range between 5 and 40 °C. The infrared camera was switched on several hours before the test in order to stabilize its internal temperature. The surface emissivity was set at 0.94, according to the measurements on a similar material in Charlès and Le Cam (2020).

5 Results

5.1 Global stretch measurement

The global stretch is determined by measuring the displacement of each grip and the initial length of the specimen. We recall here that the specimens have cylindrical ends, which avoids any slippage with the grips and makes accurate the determination of the initial length and the stretch. It should be noted that a residual strain was observed after the first cycles. This residual strain was taken into account to recalculate the stretch for the following cycles, which is consistent given that the heat source returns to zero when the stress returns to zero. An illustration is given in Figure 10, which represents the stretch level with and without correction by taking into account the residual strain in the case of the $NR_{1.2}S$ specimen.

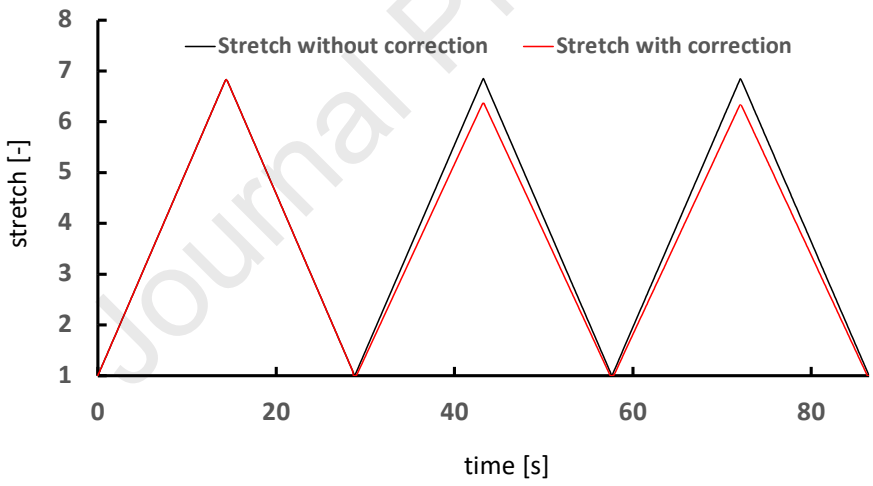

Fig. 10. Stretch level during a test (example with specimen $NR_{1.2}S$

Figure 11 presents the strain-stress response obtained for each of the four specimens during the third (stabilized) cycle. As explained above, the stretch is calculated by accounting for the residual strain, which explains that it is equal to 1 at the beginning of the third cycles. Several comments can be drawn from these results:

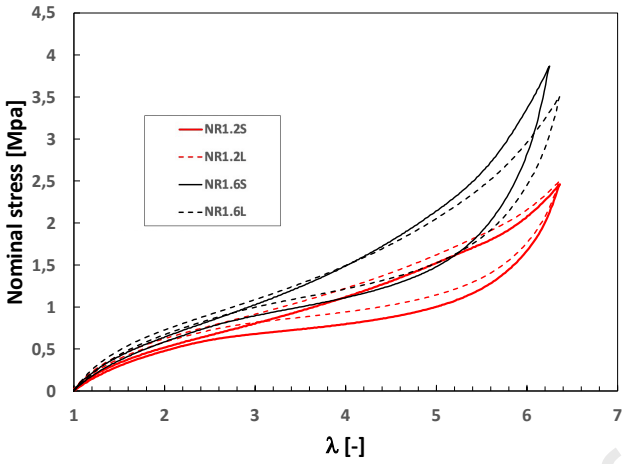

Fig. 11. Mechanical responses of small and large specimens $NR_{1.2}$ and $NR_{1.6}$.

- as expected, increasing the sulphur amount from 1.2 to 1.6 phr increases the cross-link density and therefore the material's stiffness,
- no main difference is observed between the two widths for a given sulphur amount,
- a hysteresis loop is observed in the four responses. As the material is unfilled and the maximum stretch applied is superior to that at which crystallization starts, it has been shown that the hysteresis loop is due to SIC for the most part (Samaca Martinez *et al.*, 2013b; Le Cam, 2017),
- the hysteresis loops close at a stretch of about 2.5 and under this stretch level the load and unload curves superimpose.

5.2 Thermal and calorimetric measurement at the specimens' centre

The crystallinity at the specimens's centre was determined from the methodology described in Section 3. For that purpose, the temperature measured is averaged over a zone of area equal to 0.66 and 0.68 mm^2 for small and large specimens, respectively. The evolution of the averaged temperature variations in these zones during the test corresponds to the solid lines in Figs 12 (a), (c), (e) and (g).

It was observed that these temperature variations have been evolving similarly whatever the width and the sulphur amount and reach a maximum value between 7 and 9 $°C$. Moreover, the mean temperature decreases from one cycle to another and stabilizes at the third cycle. Such evolution shows that the intrinsic dissipation has a very low contribution to the thermal response. The reader can refer to Balandraud and Le Cam (2014) for further information. A strong change in the curve slope, highlighted by the red solid lines, is observed at times corresponding to stretches ranging between 4 and 5. This result is

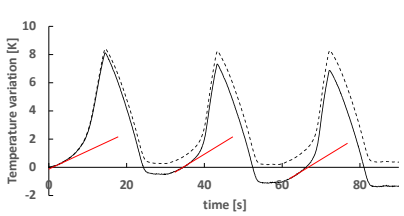

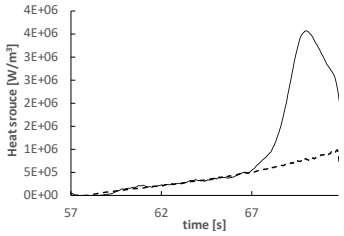

(a) Average temperature variation in $NR_{1.2}S$ (b) Average heat source in $NR_{1.2}S$

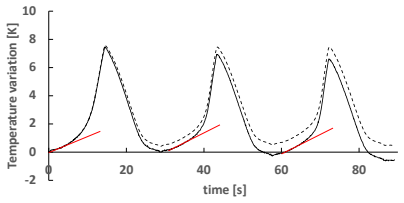

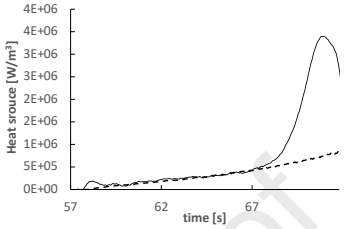

(c) Average temperature variation in $NR_{1.2}L$ (d) Average heat source in $NR_{1.2}L$

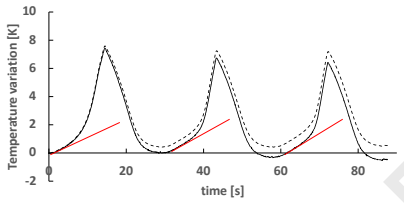

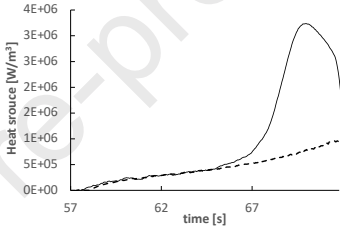

(e) Average temperature variation in $NR_{1.6}S$ (f) Average heat source in $NR_{1.6}S$

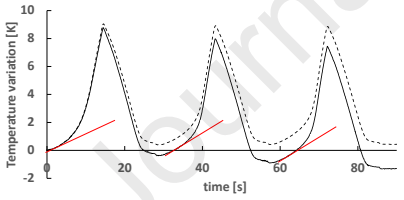

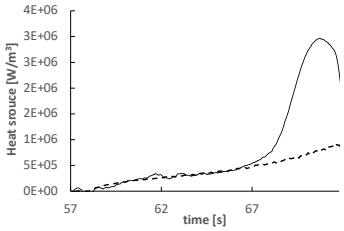

(g) Average temperature variation in $NR_{1.6}L$ (h) Average heat source in $NR_{1.6}L$

Fig. 12. Average temperature and heat source for the third stabilized cycles: (a)(c)(e)(g) non-adiabatic (measured, in solid line) and adiabatic (predicted, in dashed line) average temperatures, (b)(d)(f)(h) average heat source measured (in solid line) and predicted (in dashed line).

in a good agreement with thermal measurements performed with crystallizing unfilled natural rubbers under similar non-adiabatic conditions in the literature (Samaca Martinez *et al.*, 2013a; Le Cam, 2018; Le Cam *et al.*, 2020). The temperature variations have then been processed with the simplified formulation of the heat diffusion equation (Eq. 5) in order to determine the heat source. τ_0 has been characterized for each test, as the heat exchanges with the

specimen outside can slightly differ from one test to another even for close values of specimen widths.

From the heat sources, the corresponding adiabatic temperature variations have been determined and appear in dashed lines in the figure. As previously explained, it is observed that a slight intrinsic dissipation is produced during the first cycle (the adiabatic temperature at the end of the first cycle is superior to that at the beginning) and that the adiabatic temperature variations are then stabilized. The fact that the adiabatic temperature at the beginning and the end of the third cycles is the same means that the third cycle is a thermodynamic one and that the hysteresis loop in the mechanical response is only due to thermomechanical couplings, here SIC. Then, the crystallinity is evaluated for the third load of each test by using the methodology presented in Section 3.4. The calorimetric response without SIC has been predicted with a polynomial whose coefficients have been identified from the heat source response before SIC starts (see further details in Le Cam (2018)). Here, this corresponds to times where the stretch ranges between 1 and 3.5. Figs 12 (b), (d), (f) and (h) shows the measured (solid line) and predicted (dashed line) heat sources. The area in between is the thermal energy of SIC, which can be converted into crystallinity by applying Equation 6. One can see that this area appears the smallest for the largest specimens of each sulphur amount.

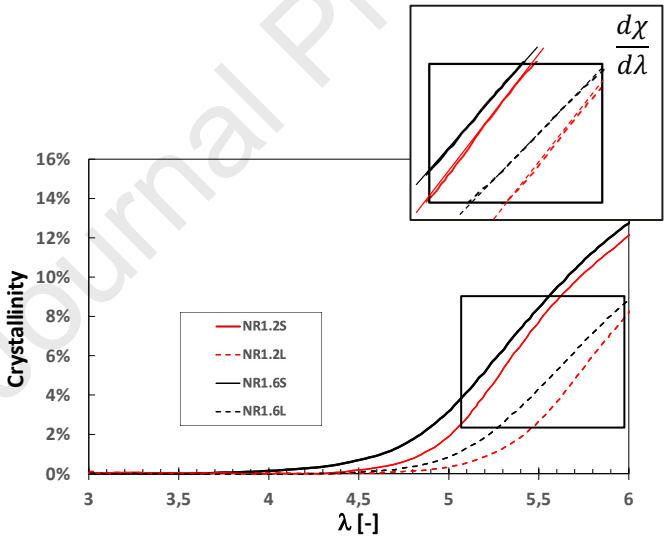

Fig. 13. Average crystallinity for the 4 specimens. The small specimens exhibit a higher crystallinity than the large ones. The higher the sulphur amount, the higher the crystallinity whatever the specimen width.

Figure 13 gathers the crystallinity (χ, in %) versus stretch in the case of the third mechanical load for the two sulphur amounts and the two geometries. The crystallinity reached at $\lambda = 6$ was equal to 12.46%, 12.19%, 8.88% and 8.11% for specimens $NR_{1.6}S$, $NR_{1.2}S$, $NR_{1.6}L$ and $NR_{1.2}L$, respectively. Thus, the highest crystallinity is obtained for the smallest width and for a given geometry, the material with the highest sulphur amount reached the

highest crystallinity. In fact, the maximum crystallinities for a given geometry are close, the largest difference is obtained in terms of crystallinity onset and crystallinity rate ($\frac{d\chi}{d\lambda}$). The fact that the crystallinity rate was found the highest for the $NR_{1.2}$ specimens is in a good agreement with the literature. As mentioned in the introduction section, Chenal *et al.* (2007) showed that a maximum crystallinity rate is observed for ν equal to 1.40 10^{-4} mol/cm^3 ($NR_{1.2}$ in the present study). The authors also correlated this result with data extracted from Trabelsi *et al.* (2003). The values are summed up in Table 3. The specimen's geometry, here the width, affects the crystallinity whatever

	Crystallinity (%) at $\lambda = 6$	Crystallization onset	$\frac{d\chi}{d\lambda}$
$NR_{1.2}S$	12.19	4.4	0.130
$NR_{1.2}L$	8.11	4.6	0.110
$NR_{1.6}S$	12.46	3.9	0.096
$NR_{1.6}L$	8.88	4.5	0.089

Table 3
Maximum crystallinity, crystallization onset and crystallinity rate for the 4 tested specimens

the sulphur amount. For the largest widths, the crystallinity was lower and SIC started at a larger stretch. Also, the crystallinity rate is lowered. This may be explained by the fact that strain field, especially the biaxiality field, is not homogeneous and is different from uniaxial tension at the specimens' centre (where the thermal measurement is carried out), which is expected when increasing the specimen's width. To further discuss on this effect, finite element calculations were performed in order to determine the maximum stretch and the biaxiality coefficient B in the specimens at a global stretch equal to 4 and to compare them according to the specimen width (see Figures 14 and 15). For the smallest specimens, the strain state is uniaxial tension and the maximum principal stretch is almost contant along the profiles. For the largest specimens, shear is induced in the middle section, with very close values of the maximum principal stretch. This is the aim of the next paragraph.

5.3 1D crystallinity field

Motivated by several observations done in our group at the macroscopic scale and reported in the first part of the present paper, we think that the crystallinity changes from one point to another in a given specimen, even though the strain field is homogeneous at the macroscopic scale. In other words the crystallinity takes place heterogeneously at the macroscopic scale. In the present study, the crystallinity is determined from temperature fields and can therefore be evaluated simultaneously at different points of the surface ob-

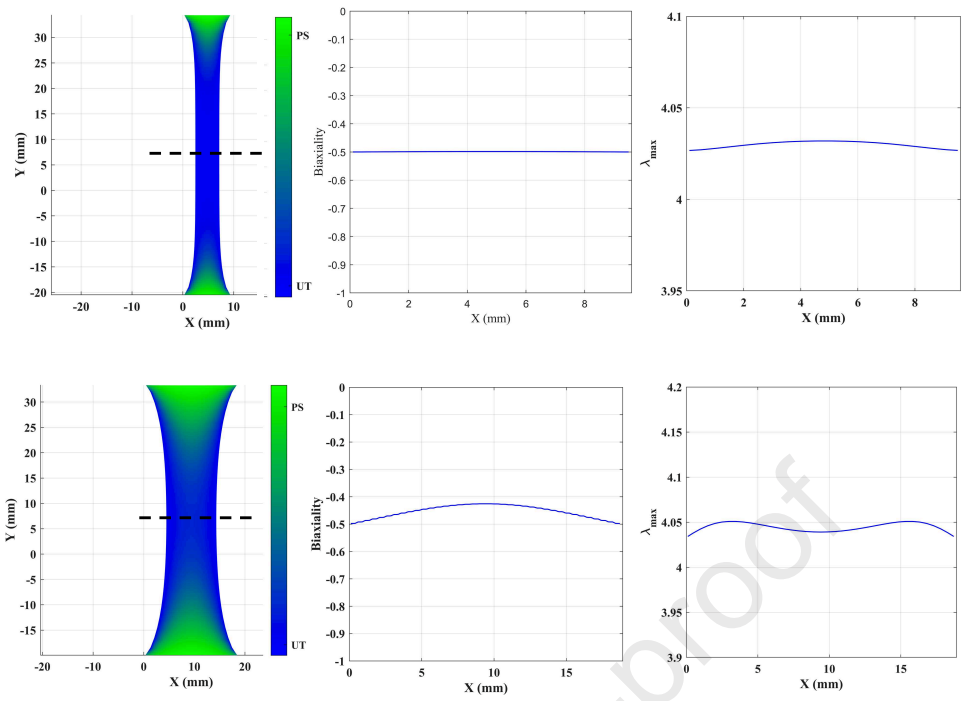

Fig. 14. Finite element simulations at a global stretch of 4 for the 2 geometries of $NR_{1.2}$. The biaxiality coefficient is mapped and its value as well as the maximal principal stretch are plotted along the profile in dashed line in the middle of the specimens.

served. Here, the crystallinity has been evaluated along profiles at the specimens' middle. The profiles include 14 measurement points (IR pixels), uniformly distributed along the specimen's width. The two on both sides of the profiles have been removed in order to avoid any border effect. Each point is represented with a different color to distinguish the different heat source (and corresponding crystallinity measurements) from the others. First of all, due to large deformations, it is necessary to check that for a given focal distance, thermal measurement zones do not superimpose in the IR pixels. Figure 16 compares the distance between two measurement points during the test with the spatial resolution of the camera (the horizontal line in black color in the figure) in the case of the lowest specimen width ($NR_{1.6}S$). It is clearly shown that the minimal distance between two measurement points remains higher than the spatial resolution, which means that the temperature measurement of each material point is independent from the others.

Figure 17 presents the heat source determined at the 14 points along the profile for the four specimens. It should be noted that in the local form of the heat diffusion equation (Eq. 1), the temperature, the stretch and the biaxiality coefficient (for calculating τ) are required at each material point. We showed

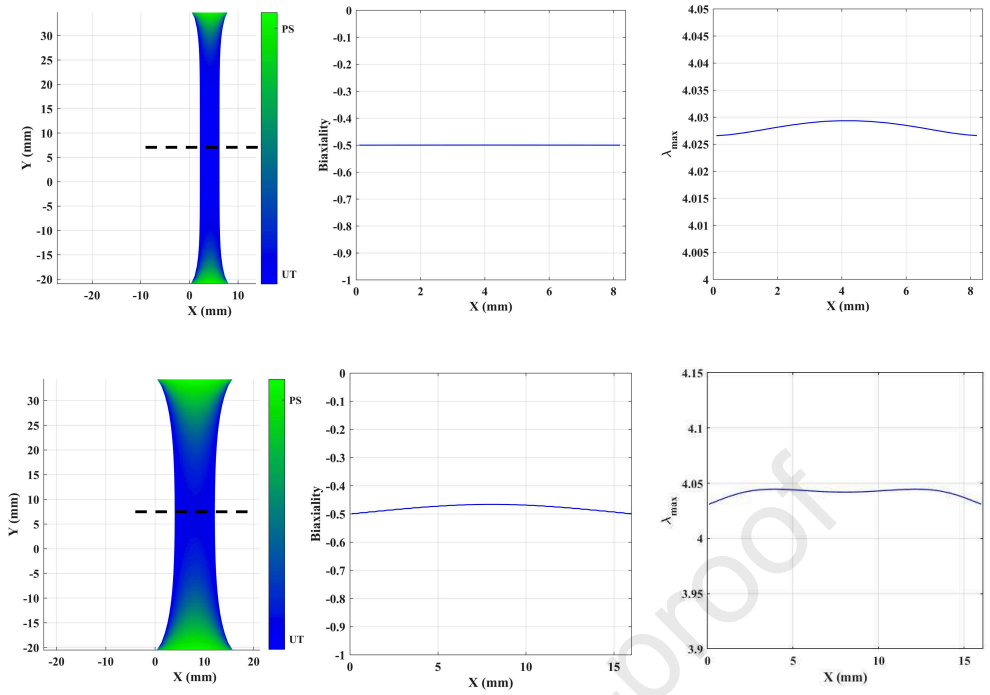

Fig. 15. Finite element simulations at a global stretch of 4 for the 2 geometries of $NR_{1.6}$. The biaxiality coefficient is mapped and its value as well as the maximal principal stretch are plotted along the profile in dashed line in the middle of the specimens.

by using the finite element analysis that the strain field is almost homogeneous, especially in the central zone where the measurements were carried out. Therefore, the same values of the stretch and the biaxiality coefficient were considered for calculating the heat source at the 14 measurement points. This figure shows that for stretches inferior to the SIC onset, the heat sources are almost superimposed for each specimen. This is consistent with the fact that under homogeneous strain field, the heat source field due to coupling between temperature and strain is homogeneous. The curve in black color is the prediction of the heat source due to this coupling only. This is shown in the crystallinity curves of Figure 18, determined from the methodology proposed in Le Cam (2017), which evidences that once the SIC onset is exceeded, the experimental heat sources evolve differently from one point to another: either the crystallinity rate $\frac{d\chi(\%)}{d\lambda}$ is different, or the SIC onset is different or both. This difference is even more significant for the large specimens. In order to visualize the distribution of the crystallinity along the profile during the test, the crystallinity profiles are given for each specimen at a global stretch equal to 4.5, 5, 5.5 and 6 in Figure 19. The biaxiality and the maximum principal stretch at the $\lambda = 6$ are also provided. The temperature and heat source profiles are given in Appendices A and B.

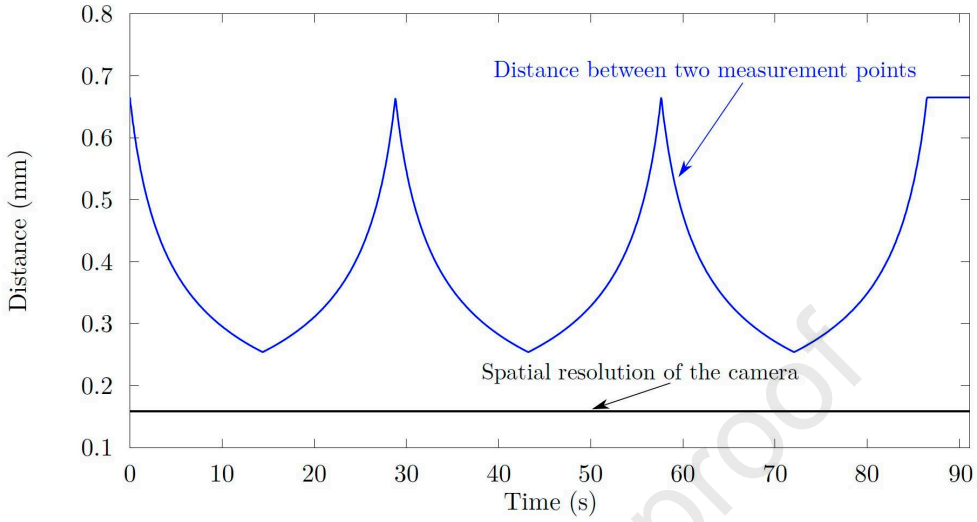

Fig. 16. Evolution of the distance between two measurement points during the test, in the case of the smallest initial distance between points (specimen $NR_{1.6}S$). At the maximum stretch applied, the distance between two points remains superior to the spatial resolution of the camera.

At $\lambda = 4.5$, crystallinity is inferior to 1% in the four specimens. Then, it increases significantly from $\lambda = 5.5$ on and becomes more and more heterogeneous. The heterogeneity is such that a difference up to 5% in the crystallinity value is observed in specimen $NR_{1.6}L$, which can not be explained by the deformation state. At the scale of the macromolecular network, some authors distinguish several crystallite families in terms of size and/or type under a homogeneous macroscopic strain field. Our measurements at the macroscopic scale do not enable us to discuss this point, however we highlight that even at the macroscopic scale under homogeneous strain field, different calorimetric signature of SIC is obtained. Considering the crystallinity rate and the SIC onset, 4 to 6 families in terms of calorimetric response can be distinguished qualitatively from these figures. These results show that heterogeneous SIC can take place while the macroscopic strain field is homogeneous, which obviously justifies taking precautions to analyze the results of the previous section considering that, similarly to the X-ray diffraction technique, the crystallinity was determined in one zone only, and pleads therefore in favor of analyzing

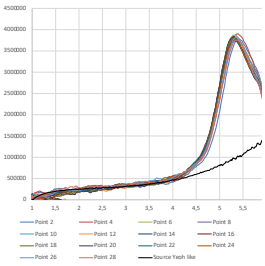

(a) $NR_{1.2}S$

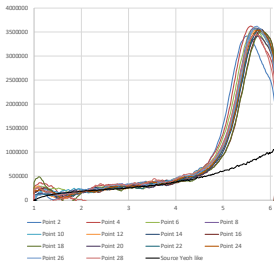

(b) $NR_{1.2}L$

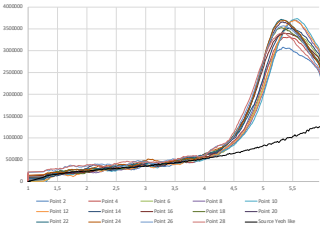

(c) $NR_{1.6}S$

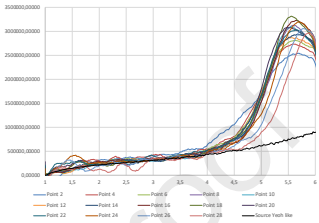

(d) $NR_{1.6}L$

Fig. 17. Heat source along the profile in the middle section.

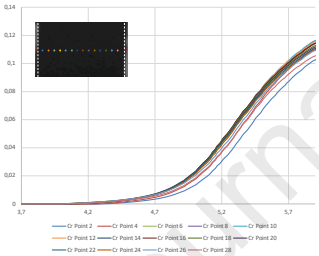

(a) $NR_{1.2}S$

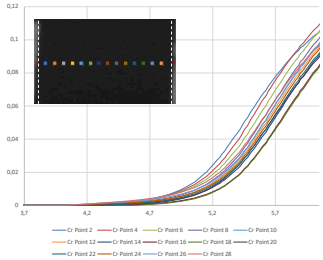

(b) $NR_{1.2}L$

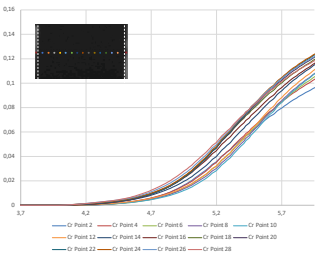

(c) $NR_{1.6}S$

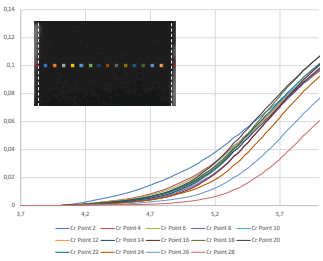

(d) $NR_{1.6}L$

Fig. 18. Crystallinity along the profile in the middle section.

SIC heterogeneity with a 2D approach. In the last part of this paper, the SIC heterogeneity is investigated through the thermal fields.

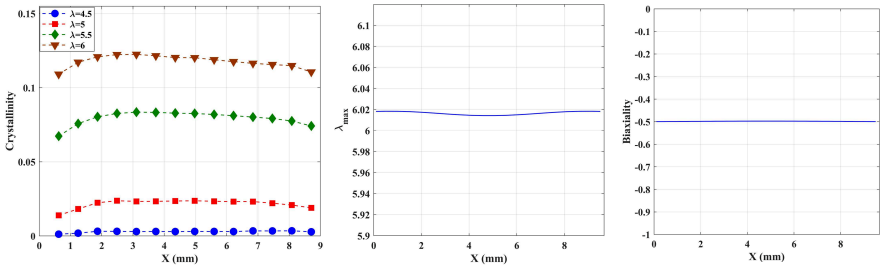

(a) $NR_{1.2}S$

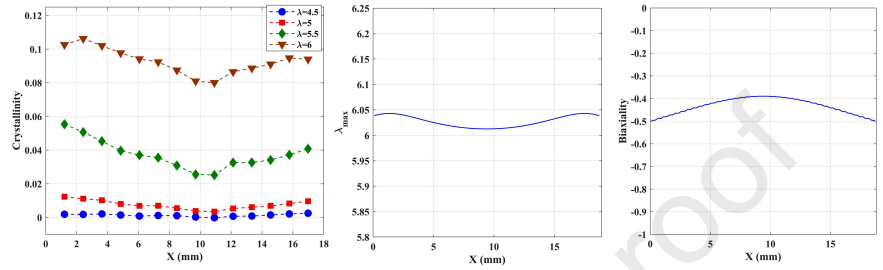

(b) $NR_{1.2}L$

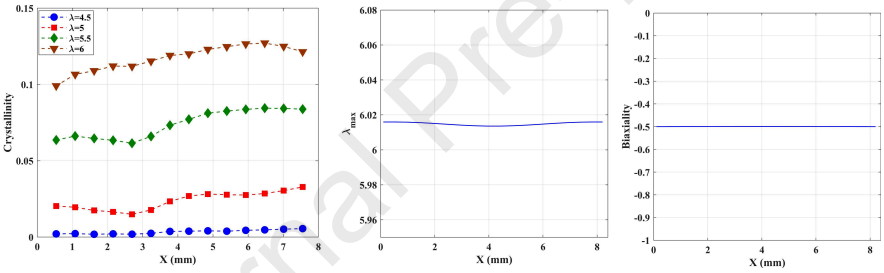

(c) $NR_{1.6}S$

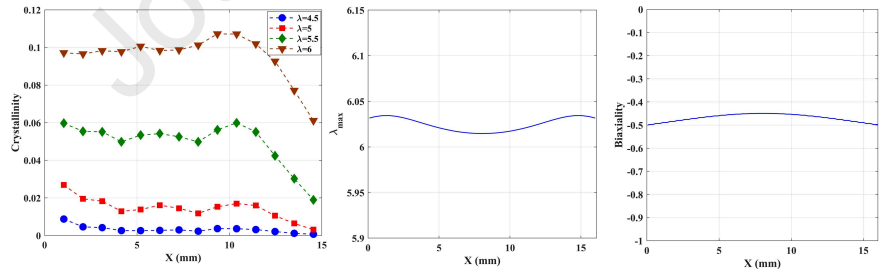

(d) $NR_{1.6}L$

Fig. 19. Crystallinity along the profile in the middle section at four increasing global stretches applied.

5.4 2D analysis of SIC heterogeneity from temperature fields

Figures 20, 21, 22 and 23 present the temperature field at different times during the four tests. First of all, we focus on the third (stabilized) loads, for

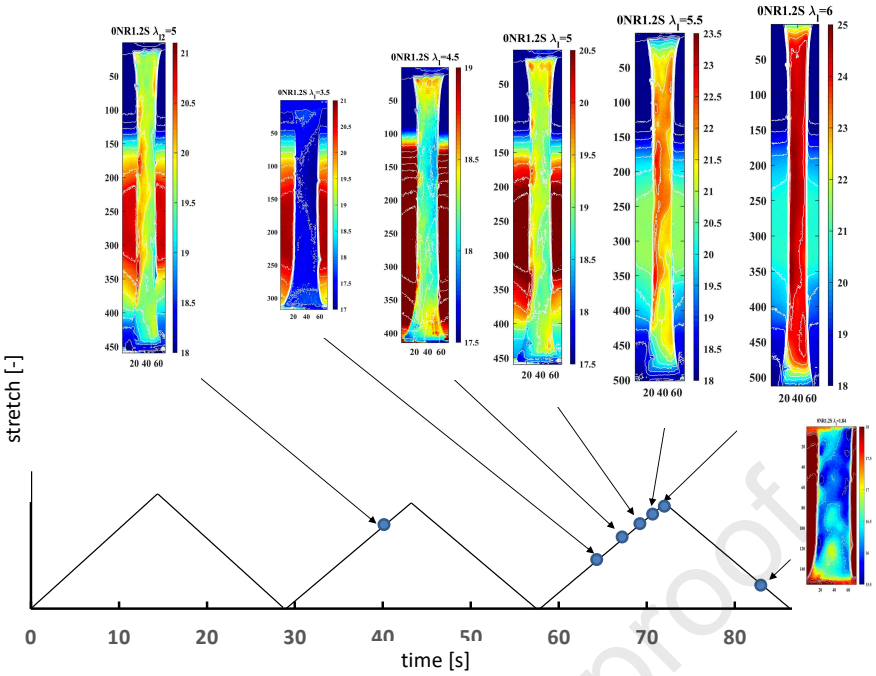

Fig. 20. $NR_{1.2}S$

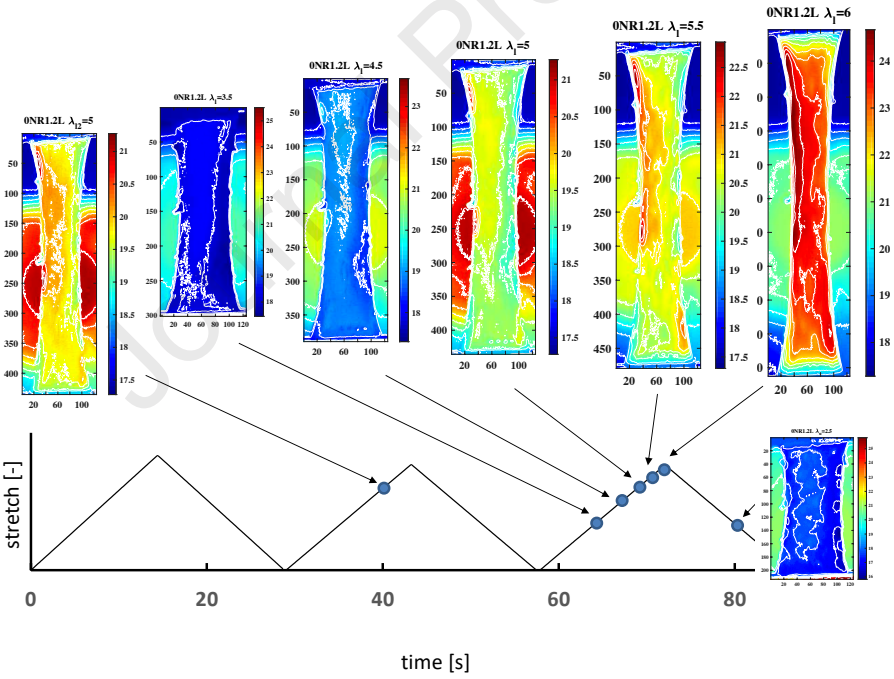

Fig. 21. $NR_{1.2}L$

which temperatures fields are presented for five increasing stretches; 3.5, 4.5, 5, 5.5 and 6 . It is first observed that for stretches inferior to the SIC onset, typically stretches of 3.5, the temperature fields are almost homogeneous as they are only due to coupling between temperature and strain. This also

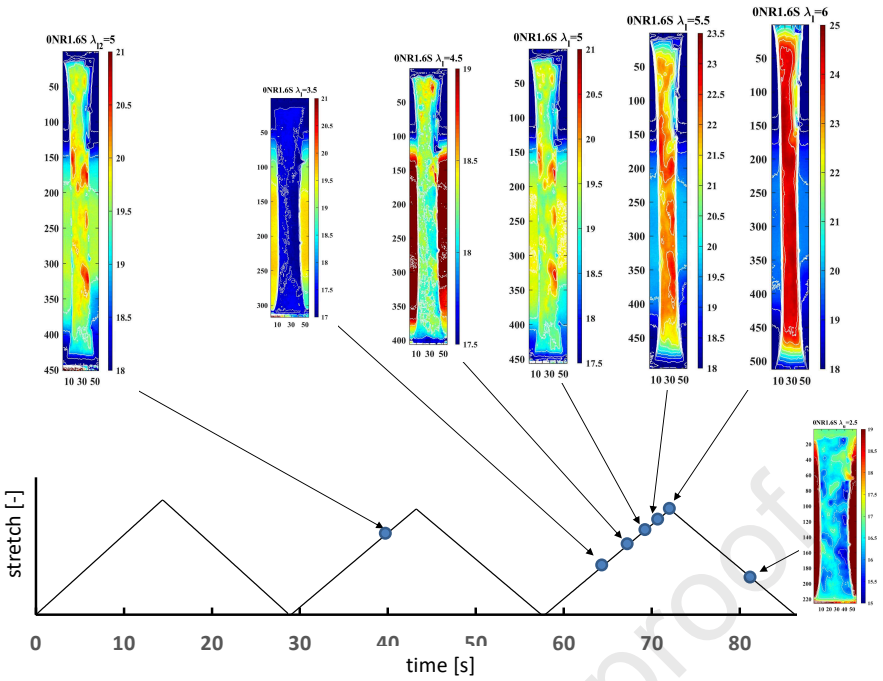

Fig. 22. $NR_{1.6}S$

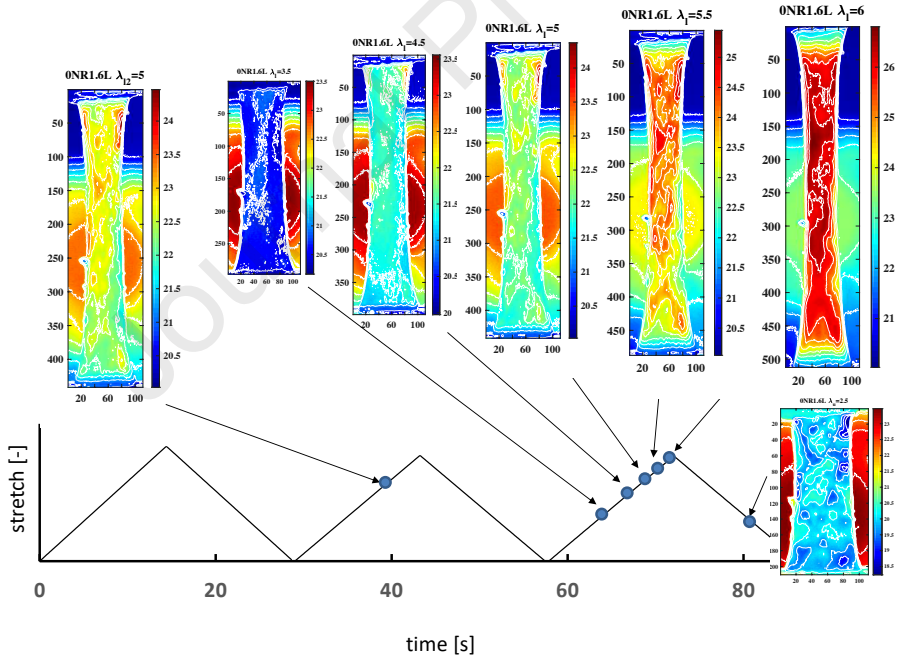

Fig. 23. $NR_{1.6}L$

shows that the surface optical properties, especially the surface emissivity, are homogeneous. Once SIC starts, the temperature fields become heterogeneous, whatever the specimen considered. The temperature gradient reaches $2°C$ at $\lambda = 6$. Moreover, comparing the temperature field in the middle of the speci-

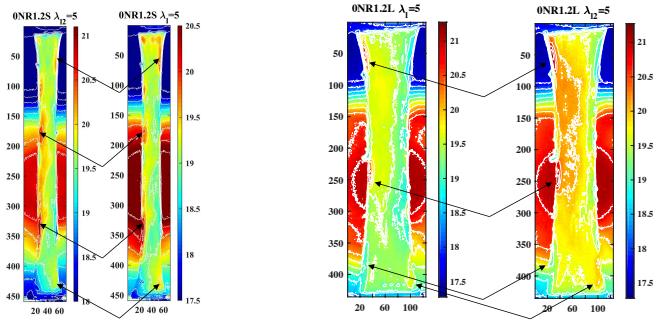

(a) $NR_{1.2}S$ (b) $NR_{1.2}L$

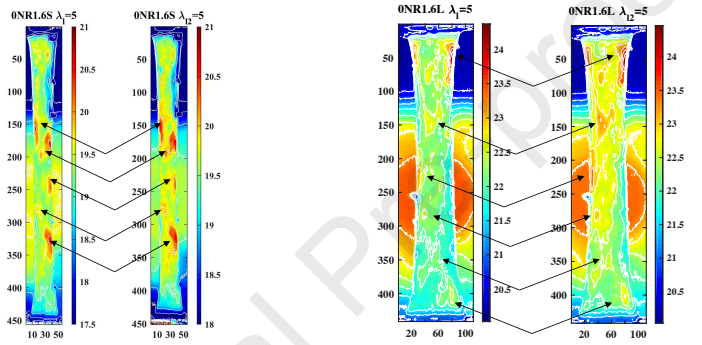

(c) $NR_{1.6}S$ (d) $NR_{1.6}L$

Fig. 24. Comparison between temperature fields at $\lambda = 5$ during the second and third loads.

mens with the profiles plotted in Figure 19 leads to consistent results, which confirms that the SIC heterogeneity at the macroscopic scale is not governed by the slight differences in the strain state.

Figure 24 compares temperature fields at a stretch equal to 5 during the second and third loads. This figure clearly shows that the thermal signature due to SIC for the second and third loads are the same. In addition, the temperature field corresponding to the melting during the last unloads can be compared to the previous temperature fields. By resizing them, it is possible to show that the zones crystallizing first are the ones melting first. These results strongly echo those suggested by Candau *et al.* (2014) on the memory effect of SIC at the scale of the macromolecular network, but for the first time at the macroscopic scale.

6 Conclusion

In this study, preliminary observations with the infrared thermography technique carried out during biaxial tests clearly highlight that SIC heterogeneity and memory effects can be observed in macroscopic zones where the strain state is homogeneous. The paper has fully investigated this effect with dedicated cyclic uniaxial tensile tests with unfilled natural rubber, coupled with infrared thermography measurements. Two specimen widths and two sulphur amounts have been considered. The thermal fields have been processed with the heat diffusion equation to determine the corresponding heat source fields. The crystallinity is then deduced from the heat source by applying a new technique developed in our laboratory. This technique is well suitable as crystallinity can be obtained satisfactorily from the heat source variation simultaneously at any point ((Le Cam, 2018; Le Cam *et al.*, 2020). It is therefore more suitable than the XRD technique to investigate SIC heterogeneity at the macroscopic scale.

The crystallinity has firstly been averaged over a zone in the middle of the specimens. The highest crystallinity was obtained for the smallest width and for a given geometry, the material with the highest sulphur amount reached the highest crystallinity. The maximum crystallinities for a given geometry were close, the largest difference was obtained in terms of crystallinity onset and crystallinity rate ($\frac{d\chi}{d\lambda}$). The maximum crystallinity rate was obtained for the sulphur amount ($1.2\ phr$) corresponding to a macromolecular network density equal to $1.40\ 10^{-4}\ mol/cm^3$, which correlates previous results reported in the literature.

Crystallinity has secondly been determined along profiles including 14 measurement points (IR pixels), uniformly distributed along the specimen's width. For stretches inferior to the SIC onset, the heat sources at each measurement points are almost superimposed for each specimen. Once the SIC onset is exceeded, the heat sources evolve differently from one point to another. In terms of crystallization, either its rate is different, or its onset is different, or both. This difference was found more significant for the largest specimen widths. Considering the crystallinity rate and the SIC onset, 4 to 6 families can be distinguished qualitatively from the calorimetric responses. These results show that heterogeneous SIC can take place while the macroscopic strain field is homogeneous, which obviously justifies taking precautions to analyze the results issued from only one measurement point or averaged over a large zone in a specimen.

A 2D analysis has thirdly been carried out with the temperature field recorded at different times during the four tests. As expected, the temperature fields were found almost homogeneous for stretches inferior to the SIC onset as they

are only due to coupling between temperature and strain. Once SIC starts, the temperature fields become heterogeneous, whatever the specimen considered. This result generalizes in 2D what was highlighted along one profile.

These results have many consequences for analyzing the local energy behavior and strength of elastomers, especially for fracture mechanics, and to link manufacturing process effects to local changes in the compound's properties.

7 Acknowledgements

The authors acknowledge the "Manufacture Française des pneumatiques Michelin" for providing the specimens for the uniaxial tension tests and J. Caillard and D. Colombo for the fruitful discussions. K. Loos, M. Johlitz and A. Lion from Institut für Mechanik (Universität der Bundeswehr, München, Germany) are acknowledged for providing the heat capacity and mass density measurement.

References

Albouy, P.-A., Guillier, G., Petermann, D., Vieyres, A., Sanseau, O., and Sotta, P. (2012). A stroboscopic X-ray apparatus for the study of the kinetics of strain-induced crystallization in natural rubber. *Polymer*, **53**(15), 3313–3324.

Albouy, P.-A., Vieyres, A., Perez-Aparicio, R., Sanseau, O., and Sotta, P. (2014). The impact of strain-induced crystallization on strain during mechanical cycling of cross-linked natural rubber. *Polymer*, **55**(16, SI), 4022–4031.

Balandraud, X. and Le Cam, J. B. (2014). Some specific features and consequences of the thermal response of rubber under cyclic mechanical loading. *Archive of Applied Mechanics*, **84**(6), 773–788.

Bastos, G., Sales, L., Di Cesare, N., Tayeb, A., and Le Cam, J.-B. (2021). Inverse-pagerank-pso for inverse identification of hyperelastic models: a feasibilty study. *Journal of Rubber Research*, **24**, 447–460.

Berthel, B., Chrysochoos, A., Wattrisse, B., and Galtier, A. (2008). Infrared image processing for the calorimetric analysis of fatigue phenomena. *Experimental Mechanics*, **48**, 79–90.

Beurrot, S., Huneau, B., and Verron, E. (2010). In situ sem study of fatigue crack growth mechanism in carbon black-filled natural rubber. *Journal of Applied Polymer Science*, **117**, 1260–1269.

Beurrot, S., Huneau, B., and Verron, E. (2011). Strain-induced crystallization of natural rubber subjected to biaxial loading conditions as revealed by x-ray

diffraction. In *7th European Conference on Constitutive Models for Rubber; Jerrams, S., Murphy, N., Eds.; Taylor & Francis Group, 2012*, pages 23–28.

Bunn, C. (1942). . *Proc. R. Soc. London, Ser. 1*, **180**, 40.

Cadwell, S. M., Merril, R. A., Sloman, C. M., and Yost, F. L. (1940). Dynamic fatigue life of rubber. *Industrial and Engineering Chemistry (reprinted in Rubber Chem. and Tech. 1940;13:304-315)*, **12**, 19–23.

Candau, N., Laghmach, R., Chazeau, L., Chenal, J.-M., Gauthier, C., Biben, T., and Munch, E. (2014). Strain-induced crystallization of natural rubber and cross-link densities heterogeneities. *Macromolecules*, **47**(16), 5815–5824.

Charlès, S. and Le Cam, J.-B. (2020). Inverse identification from heat source fields: a local approach applied to hyperelasticity. *Strain*, **https://doi.org/10.1111/str.12334**, e12334.

Chen, X., Meng, L., Zhang, W., Ye, K., Xie, C., Wang, D., Chen, W., Nan, M., Wang, S., and Li, L. (2019). Frustrating strain-induced crystallization of natural rubber with biaxial stretch. *ACS Applied Materials & Interfaces*, **11**(50), 47535–47544.

Chenal, J.-M., Chazeau, L., Guy, L., Bomal, Y., and Gauthier, C. (2007). *Polymer*, **48**, 1042–1046.

Chrysochoos, A. (1995). Analyse du comportement des matériaux par thermographie infra rouge. In *Colloque Photomécanique*, volume 95, pages 201–211.

Chrysochoos, A., Huon, V., Jourdan, F., Muracciole, J., Peyroux, R., and Wattrisse, B. (2010). Use of full-field digital image correlation and infrared thermography measurements for the thermomechanical analysis of material behaviour. *Strain*, **46**, 117–130.

Flory, P. J. (1947). Thermodynamics of crystallization in high polymers. i. crystallization induced by stretching. *The Journal of Chemical Physics*, **15**, 397–408.

Goppel, J. and Arlman, J. (1949). . *Appl. Sci. Res. Sect. A*, **1**, 462.

Guélon, T., Toussaint, E., Le Cam, J.-B., Promma, N., and Grédiac, M. (2009). A new characterization method for rubbers. *Polymer Testing*, **28**, 715–723.

Huneau, B. (2011). Strain-induced crystallization of natural rubber: a review of X-ray diffraction investigations. *Rubber Chemistry And Technology*, **84**(3), 425–452.

Ikeda, Y., Higashitani, N., Hijikata, K., Kokubo, Y., Morita, Y., Shibayama, M., Osaka, N., Suzuki, T., Endo, H., and Kohjiya, S. (2009). Nonuniformity in cross-linked natural rubber as revealed by contrast-variation small-angle neutron scattering. *Macromolecules*, **42**, 2741–2748.

Immirzi, A., Tedesco, C., Monaco, G., and Tonelli, A. (2005). Crystal structure and melting entropy of natural rubber. *Macromolecules*, **38**, 1223.

Johlitz, M. and Diebels, S. (2011). Characterisation of a polymer using biaxial tension tests. part i: Hyperelasticity. *Arch Appl. Mech.*, **81**, 1333–1349.

Katz, J. (1925). *Naturw*, **4**, 169.

Khiem, V., Le Cam, J.-B., Charlès, S., and Itskov, M. (2022). Thermodynamics of strain-induced crystallization in filled natural rubber under uni- and biaxial loadings. part i: complete energetic characterization and crystallinity

evaluation. *Journal of the Mechanics and Physics of Solids*, **159**, 104701.

Kohjiya, S., Tosaka, M., Masahiro, M., Ikeda, Y., Toki, S., and Hsiao, B. S. (2007). Role of stearic acid in the strain-induced crystallization of crosslinked natural rubber ans synthetic cis-1,4-polyisoprene. *Polymer*, **48**, 3801–3808.

Le Cam, J.-B. (2017). Energy storage due to strain-induced crystallization in natural rubber: the physical origin of the mechanical hysteresis. *Polymer*, **127**, 166–173.

Le Cam, J.-B. (2018). Strain-induced crystallization in rubber: A new measurement technique. *Strain*, **54**(1), e12256.

Le Cam, J.-B. and Toussaint, E. (2010). The mechanism of fatigue crack growth in rubbers under severe loading: the effect of stress-induced crystallization. *Macromolecules*, **43**, 4708–4714.

Le Cam, J.-B., Huneau, B., Verron, E., and Gornet, L. (2004). Mechanism of fatigue crack growth in carbon black filled natural rubber. *Macromolecules*, **37**, 5011–5017.

Le Cam, J.-B., Verron, E., and Huneau, B. (2008). Description of fatigue damage in carbon black filled natural rubber. *Fatigue and Fracture of Engineering Materials & Structures*, **31**, 1031–1038.

Le Cam, J.-B., Huneau, B., and Verron, E. (2013). Fatigue damage in carbon black filled natural rubber under uni- and multiaxial loading conditions. *International Journal of Fatigue*, **52**, 82 – 94.

Le Cam, J. B., Albouy, P.-A., and Charlès, S. (2020). Comparison between x-ray diffraction and quantitative surface calorimetry based on ir thermography to evaluate strain-induced crystallinity in natural rubber. *Review of Scientific Instruments*, **91**, 044902.

Louche, H. (2009). *Etudes de certains phénomènes de localisation à partir de champs thermomécaniques*. Habilitation thesis, Savoie University.

Marchal, J. (2006). *Cristallisation des caoutchoucs chargés et non chargés sous contrainte : Effet sur les chaînes amorphes*. PhD Thesis, Université Paris XI Orsay, France.

Poompradub, S., Tosaka, M., Kohjiya, S., Ikeda, Y., and Tokiand I. Sics, S. (2005). Mechanism of strain-induced crystallization in filled and unfilled natural rubber vulcanizates. *Journal of Applied Physics*, **97**, 103529/1–103529/9.

Promma, N., Raka, B., Grédiac, M., Toussaint, E., Le Cam, J.-B., Balandraud, X., and Hild, F. (2009). Application of the virtual fields method to mechanical characterization of elastomeric materials. *International Journal of Solids and Structures*, **46**, 698–715.

Qin, Q. and G. B. McKenna (2006). . *J. Polym. Sci. Pt. B-Polym. Phys.*, **44**(24).

Rajkumar, G., Squire, J., and Arnott, S. (2006). . *Macromolecules*, **39**, 7004.

Roberts, D. E. and Mandelkern, L. (1955). Thermodynamics of crystallization in high polymers. natural rubber. *Rubber Chemistry and Technology*, **28**(3), 718–727.

Rublon, P., Huneau, B., Saintier, N., Beurrot, S., Leygue, A., Verron, E., Mocuta, C., Thiaudière, D., and Berghezan, D. (2013). *In situ* synchrotron wide-angle X-ray diffraction investigation of fatigue cracks in natural rubber. *Journal of Synchrotron Radiation*, **20**(1), 105–109.

Rublon, P., Huneau, B., Verron, E., Saintier, N., Beurrot, S., L., A., Mocuta, C., Thiaudière, D., and Berghezan, D. (2014). Multiaxial deformation and strain-induced crystallization around a fatigue crack in natural rubber. *Engineering Fracture Mechanics*, **123**, 59 – 69.

Ruellan, B., Le Cam, J. B., Robin, E., Jeanneau, I., Canévet, F., Mauvoisin, G., and Loison, D. (2018). Fatigue crack growth in natural rubber: The role of sic investigated through post-mortem analysis of fatigue striations. *Engineering Fracture Mechanics*, **201**, 353–365.

Ruellan, B., Le Cam, J. B., Jeanneau, I., Canévet, F., Mortier, F., and Robin, E. (2019). Fatigue of natural rubber under different temperatures. *International Journal of Fatigue*, **124**, 544–557.

Saintier, N. (2000). *Prévisions de la durée de vie en fatigue du NR, sous chargement multiaxial*. Thèse de doctorat, École Nationale Supérieure des Mines de Paris.

Saintier, N., Cailletaud, G., and Piques, R. (2006). Multiaxial fatigue life prediction for a natural rubber. *International Journal of Fatigue*, **28**, 530–539.

Samaca Martinez, J. R., Le Cam, J.-B., Balandraud, X., Toussaint, E., and Caillard, J. (2013a). Thermal and calorimetric effects accompanying the deformation of natural rubber. part 1: Thermal characterization. *Polymer*, **54**, 2717 – 2726.

Samaca Martinez, J. R., Le Cam, J.-B., Balandraud, X., Toussaint, E., and Caillard, J. (2013b). Thermal and calorimetric effects accompanying the deformation of natural rubber. part 2: quantitative calorimetric analysis. *Polymer*, **54**, 2727 – 2736.

Seibert, H., Scheffer, T., and Diebels, S. (2014). Biaxial testing of elastomers - experimental setup, measurement and experimental optimisation of specimen's shape. *Technische Mechanik*, **81**, 72–89.

Suzuki, T., Osaka, N., Endo, H., Shibayama, M., Ikeda, Y., Asai, H., Higashitani, N., Kokubo, Y., and Kohjiya, S. (2010). *Macromolecules*, **43**(3), 1556–1563.

Takahashi, Y. and Kumano, T. (2004). Crystal Structure of Natural Rubber. *Macromolecules*, **37**, 4860.

Tayeb, A., Le Cam, J.-B., Grédiac, M., Toussaint, E., and Balandraud, X. (2021). Identifying hyperelastic constitutive parameters with sensitivity-based virtual fields. *Strain*, **e12397**.

Toki, S. and Hsiao, B. (2003). *Macromolecules*, **36**, 5915–5917.

Toki, S., Fujimaki, T., and Okuyama, M. (2000). Strain-induced crystallization of natural rubber as detected real-time by wide-angle x-ray diffraction technique. *Polymer*, **41**, 5423–5429.

Toki, S., Sics, I., Ran, S., Liu, L., and Hsiao, B. (2003). Molecular orienta-

tion and structural development in vulcanized polyisoprene rubbers during uniaxial deformation by in situ synchrotron x-ray diffraction. *Polymer*, **44**, 6003–6011.

Tosaka, M. (2009). A route for the thermodynamic description of strain-induced crystallization in sulfur-cured natural rubber. *Macromolecules*, **42**, 6166–6174.

Tosaka, M., Murakami, S., Poompradub, S., Kohjiya, S., Ikeda, Y., Toki, S., Sics, I., and Hsiao, B. S. (2004). Orientation and crystallization of natural rubber network as revealed by waxd using synchrotron radiation. *Macromolecules*, **37**, 3299–3309.

Toussaint, E., Balandraud, X., Cam, J.-B. L., and Grédiac, M. (2012). Combining displacement, strain, temperature and heat source fields to investigate the thermomechanical response of an elastomeric specimen subjected to large deformations. *Polymer Testing*, **31**, 916–925.

Trabelsi, S., Albouy, P.-A., and Rault, J. (2002). Stress-induced crystallization around a crack tip in natural rubber. *Macromolecules*, **35**, 10054–10061.

Trabelsi, S., Albouy, P., and Rault, J. (2003). Crystallization and melting processes in vulcanized stretched natural rubber. *Macromolecules*, **36**(20), 7624–7639.

Valentin, J., Posadas, P., Fernandez-Torres, A., Malmierca, M., Gonzalez, L., Chasse, W., and Saalwächter, K. (2010). nhomogeneities and Chain Dynamics in Diene Rubbers Vulcanized with Different Cure Systems. *Macromolecules*, **43**(9).

Vieyres, A., Pérez-Aparicio, R., Albouy, P.-A., Sanseau, O., Saalwächter, K., Long, D., and Sotta, P. (2013). Sulfur-cured natural rubber elastomer networks: correlating cross-link density, chain orientation, and mechanical response by combined techniques. *Macromolecules*, **46**(3), 889–899.

Yijing, N., Zhouzhou, G., Ya, W., Tongfan, H., and Zhiping, Z. (2017). Features of strain-induced crystallization of natural rubber revealed by experiments and simulations. *Polymer Journal*, **49**(3), 309–317.

A Temperature along the profile in the middle section at four increasing global stretches applied

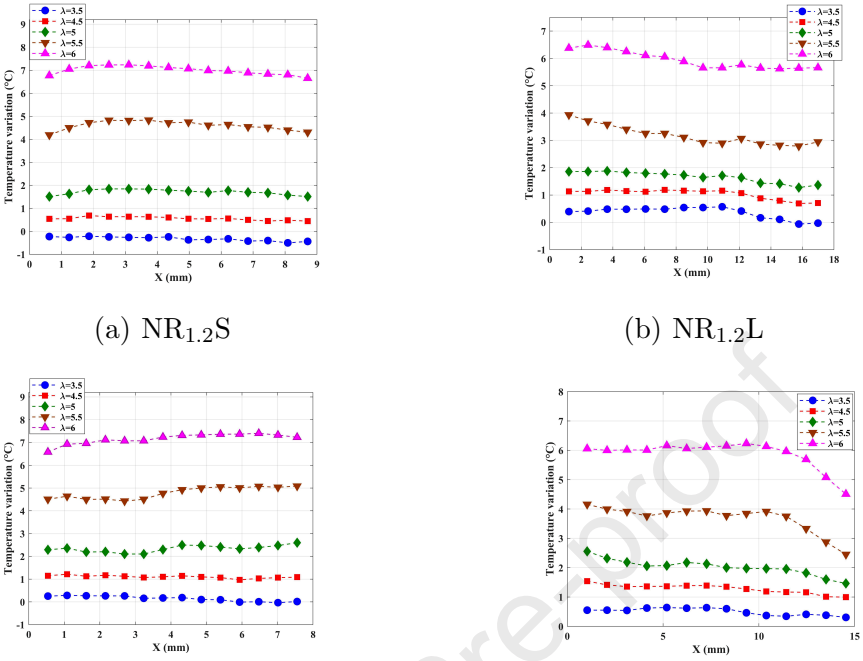

(a) $NR_{1.2}S$ (b) $NR_{1.2}L$

(c) $NR_{1.6}S$ (d) $NR_{1.6}L$

Fig. A.1. Temperature along the profile in the middle section at four increasing global stretches applied.

B Heat source along the profile in the middle section at four increasing global stretches applied

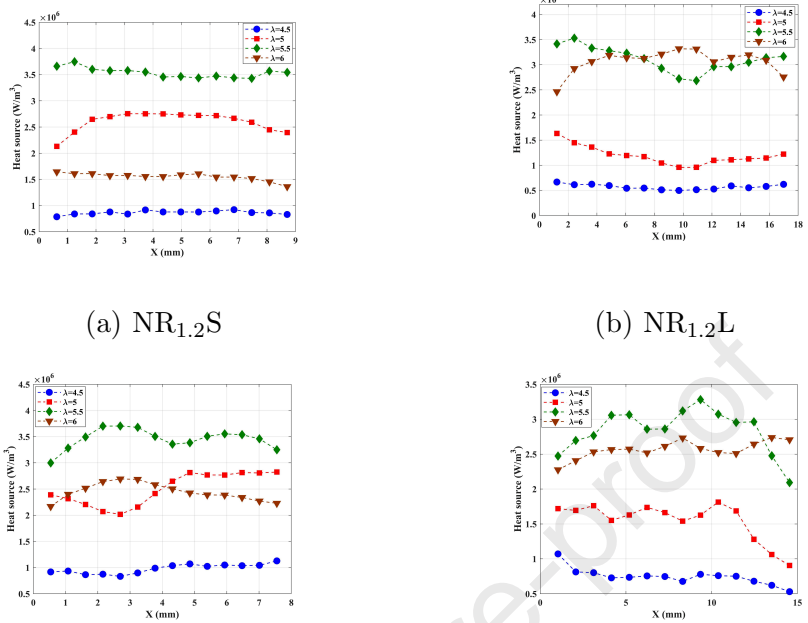

(a) $NR_{1.2}S$ (b) $NR_{1.2}L$

(c) $NR_{1.6}S$ (d) $NR_{1.6}L$

Fig. B.1. Heat source along the profile in the middle section at four increasing global stretches applied.

Highlights

Heterogeneous SIC takes place at the macroscale under homogeneous mechanical loading.
Sulfur amount and specimen geometry effects have been characterized.
The experimental technique used provides the crystallinity field instantaneously.
Several calorimetric families were distinguished in the macroscopic crystallized zones.

Declaration of interests

☐ The authors declare that they have no known competing financial interests or personal relationships that could have appeared to influence the work reported in this paper.

☒The authors declare the following financial interests/personal relationships which may be considered as potential competing interests:

Jean-Benoit LE CAM reports equipment, drugs, or supplies was provided by French Manufacture of Michelin Tyres.